

Electronic Supplementary Information for

## **Buoyancy-driven step emulsification on pneumatic centrifugal microfluidic platforms**

Liviu Clime,<sup>\*a†</sup> Lidija Malic,<sup>a†</sup> Jamal Daoud,<sup>b</sup> Luke Lukic,<sup>a</sup> Matthias Geissler<sup>a</sup>  
and Teodor Veres<sup>a</sup>

<sup>a</sup> Life Sciences Division, National Research Council of Canada, 75 de Mortagne Boulevard,  
Boucherville, QC, J4B 6Y4, Canada

<sup>b</sup> Galenvs Sciences, Inc., 24 Gabrielle-Roy Street, Montreal, QC, H3E 1M3, Canada

† These authors contributed equally to the work.

\* Corresponding author. E-mail: liviu.clime@cnrc-nrc.gc.ca

# Contents

1. Pneumatic centrifugal microfluidic platform .....	3
2. Microfluidic cartridge.....	3
3. Numerical model.....	5
4. Imaging of droplets and data analysis .....	6
5. Derivation of Eq. (8) .....	7
6. Surface tension measurements .....	8
7. References .....	11

## 1. Pneumatic centrifugal microfluidic platform

The platform (Fig. S1), which is described in more detail elsewhere,<sup>1</sup> features an integrated pumping and pressure control system to mediate the displacement of fluids on the cartridge. Pressure outlets can be programmed to either apply pressure from the pump (between  $-5$  and  $+10$  PSI) or to serve as a vent. The electronic system is designed such that all functions performed by the pump and the valves can be computer-controlled in real-time while the platform is rotating at high speed. Electrical power and computer commands are sent through a slip-ring to switch the states of the electromechanical valves with a temporal resolution of few milliseconds.



**Fig. S1** Centrifugal microfluidic platform. The photograph shows a prototype instrument during the installation of a microfluidic cartridge (unrelated to the work described in here).

## 2. Microfluidic cartridge

The microfluidic cartridge (Fig. S2) was fabricated according to published procedures<sup>2-4</sup> and assembled as a hybrid polymer stack with rectangular geometry. Mediprene OF 400M was

received in the form of pellets from Hexpol TPE (Åmål, Sweden) and was extruded at 165 °C to form sheets of several meters in length and 1 mm in thickness. An SU-8 mold was first prepared using published procedures.<sup>2</sup> An epoxy mold (Conapoxy FR-1080 resin; Cytec Industries, Woodland Park, NJ) was then produced from the SU-8/silicon master mold using an intermediate replication step with poly(dimethyl siloxane) (Sylgard 184; Dow Corning, Midland, MI).<sup>4</sup> Hot embossing of Mediprene was performed with an EVG 520 system (EV Group, Schärding, Austria) at a temperature of 120 °C, an applied force of 5 kN, and a pressure of  $10^{-2}$  mbar. A thin (125  $\mu\text{m}$ ) polycarbonate sheet (McMaster-Carr, Elmhurst, IL) was added on top of the Mediprene layer to increase rigidity and facilitate handling. The microfluidic circuit was then enclosed with a Zeonor sheet that was either obtained commercially from Zeon Chemicals (Louisville, KY) or fabricated in-house with an e-motion 110 injection molding tool (Engel, Schwertberg, Austria) using conditions that are described in detail elsewhere.<sup>5</sup> All fabrication steps were carried out in a clean room (class 1,000) environment.

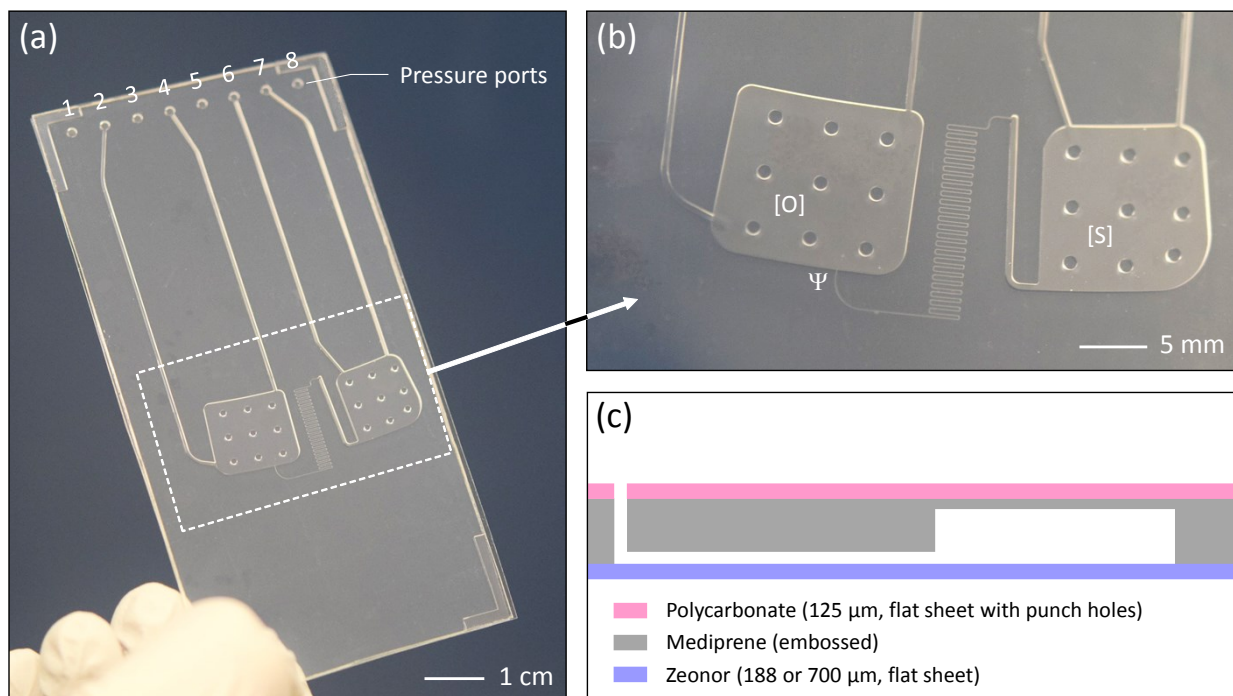


**Fig. S2** Microfluidic cartridge. (a) Photograph of the device as it was used within this work. Pressure ports are connected to the pneumatic manifold on the rotating stage of the platform. (b) Close-up view of the emulsification unit. Support posts were implemented in both reservoirs to enhance their mechanical stability. (c) Scheme (cross-

sectional view) of the hybrid, three-layer polymer structure used for the fabrication and assembly of the cartridge (not to scale).

### 3. Numerical model

All definitions for the mesh, initial fields, physical models and control parameters have been performed with OpenFOAM for Windows 18.10 ([www.openfoam.com](http://www.openfoam.com)). The computational domain consists of two rectangular blocks of  $40\ \mu\text{m} \times 40\ \mu\text{m} \times 1\ \text{mm}$  and  $2\ \text{mm} \times 2\ \text{mm} \times 500\ \mu\text{m}$  corresponding to the microfluidic channel and the reservoir for the continuous phase, respectively (labeled as block 1 and block 2 in Fig. S3). The two blocks are merged at the middle point  $\Psi$  such that they have a common interface (the bottom one) and form a structure similar to the actual microfluidic unit. The resulting computational domain is discretized in 3.4 million cells (hexahedra) and about the same number of points. The face A (Fig. S3) is defined as inlet and constant velocity boundary conditions (of `fixedValue` type) are imposed. The opposite face B (on the block 2) is considered as an outlet with pressure boundary conditions of type `pressureInletOutletVelocity`. All other faces are treated as walls and non-slip boundary conditions of type `noSlip` are imposed everywhere.

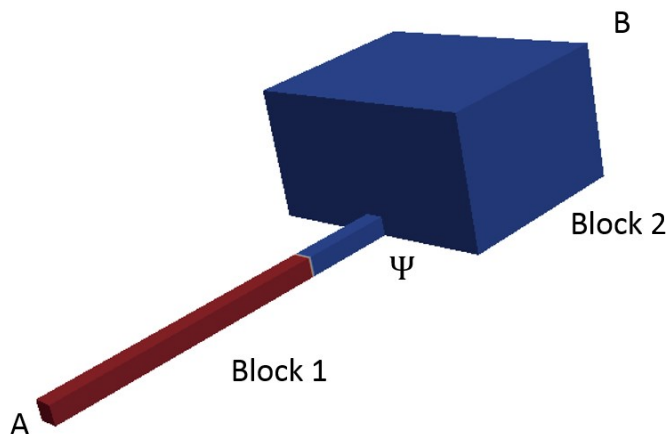


**Fig. S3** Computational domain and initial configuration of the two phases (red: sample; blue: oil). Densities of  $1,000\ \text{kg/m}^3$  and  $1,500\ \text{kg/m}^3$  as well as kinematic viscosities of  $10^6\ \text{m}^2/\text{s}$  and  $2 \times 10^6\ \text{m}^2/\text{s}$  were considered for sample and oil phase, respectively. The surface tension coefficient between these two phases has been set to  $0.03\ \text{N/m}$  with a `Newtonian` model as type of simulation. The above definitions have been transferred to the application `interFoam` for running the simulation in parallel on 20 CPUs. Using a Z820 Hewlett-Packard

workstation,  $50\text{ ms}$  of real-time physical simulation is solved in about 5 h. VTK files ([www.vtk.org](http://www.vtk.org)) are written every  $50\ \mu\text{s}$  and the simulation results were visualized using ParaView 5.0.1 software ([www.paraview.org](http://www.paraview.org)).

#### 4. Imaging of droplets and data analysis

Water-in-oil emulsions were produced using Novec 7500 Engineered Fluid ( $\rho = 1.6140\text{ g/cm}^3$ ; 3M, St. Paul, MN) containing 2% (w/v) Pico-Surf 1 (Dolomite Microfluidics, Royston, UK) as the continuous phase. They were recovered from the microfluidic cartridge using a micropipette and transferred into glass tubes with a rectangular profile (Sigma-Aldrich, Oakville, ON) so that droplets arrange into a close-packed monolayer to facilitate imaging. Bright-field images of droplets were acquired with a  $10\times$  field lens using a Ti Eclipse inverted microscope (Nikon, Melville, NY) equipped with an Andor iXon Ultra EMCCD camera (Oxford Instruments, Abingdon, UK). Droplet diameters were determined from optical micrographs using ImageJ analysis software (<https://imagej.nih.gov/ij/>), as shown by the example in Fig. S4.

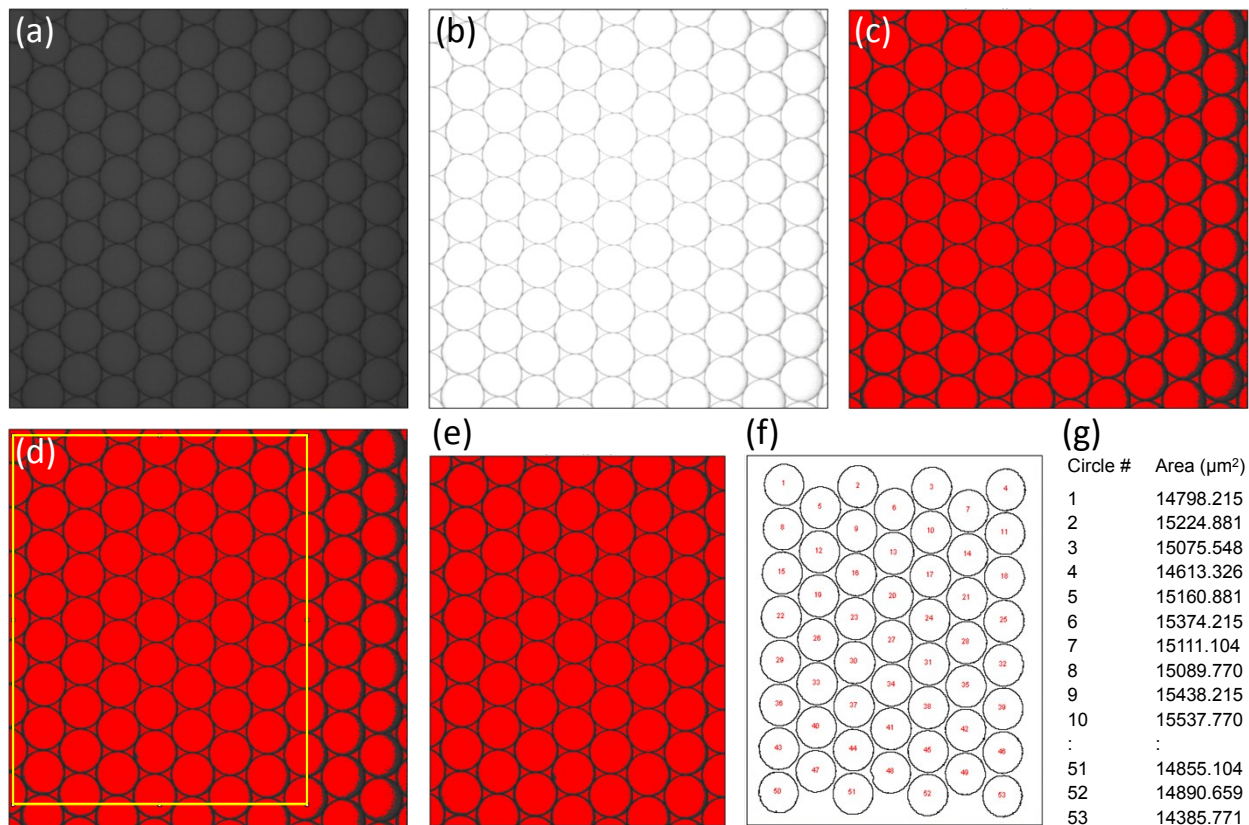


**Fig. S4** Droplet size analysis using ImageJ. (a) Gray-scale image of droplets produced at 700 rpm and 2 PSI. The scale was set to 0.375 pixels/ $\mu\text{m}$ . (b) Binary image. (c) Threshold (red) for binary image. (d) Region of interest (ROI) for the measurement (outlined in yellow). (e) Cropped ROI area. (f) Drawing of the circles in the ROI considered by the “Analyze Particles” function. (g) Output file detailing the surface area for each circle in the ROI, which was used to calculate droplet diameters.

After converting the image to a binary format, a manual threshold was defined to delineate the circles. The image was then cropped to prevent any distortion of the measurement from shadow effects deriving from non-uniform illumination. By setting circularity to 0.7–1.0, the area of each circle was computed using the “Analyze Particles” function. A total of 132 droplets were analyzed for 300 rpm and 6 PSI, 210 droplets for 500 rpm and 4 PSI, and 306 droplets for 700 rpm and 2 PSI. Droplet diameters were calculated from the circle areas in the output files and plotted in histogram format (1  $\mu\text{m}$  bin size) using SciDavis software (scidavis.sourceforge.net).

## 5. Derivation of Eq. (8)

By replacing  $Q_0$  from Eq. (4) in Eq. (7) we obtain

$$R = \sqrt{\frac{9\eta}{2\alpha\omega^2 R_\Psi \Delta\rho} \left( \frac{\Delta p_{app} + \Delta p_{cf} + \Delta p_\sigma}{Z} + \beta \right)}$$

where we denoted the centrifugal pressure difference between the oil and sample columns as  $\Delta p_{cf}$  and the Laplace surface tension as  $\Delta p_\sigma$ . By regrouping the terms in the parenthesis around  $\Delta p_{app}$  we get

$$R = \sqrt{\frac{9\eta}{2\alpha\omega^2 R_\Psi \Delta\rho Z} \Delta p_{app} + \frac{9\eta}{2\alpha\omega^2 R_\Psi \Delta\rho} \left( \frac{\Delta p_{cf} + \Delta p_\sigma}{Z} + \beta \right)}$$

which by identification with Eq. (8) provides

$$\alpha' = \frac{9\eta}{2\alpha\omega^2 R_\Psi \Delta\rho Z}$$

and

$$\beta' = \frac{9\eta}{2\alpha\omega^2 R_\Psi \Delta\rho} \left( \frac{\Delta p_{cf} + \Delta p_\sigma}{Z} + \beta \right)$$

Conversely, numerical values of the parameters  $\alpha$  and  $\beta$  can be derived from the above  $\alpha'$  and  $\beta'$  values as

$$\alpha(\omega) = \frac{9\eta}{2\alpha'\omega^2 R_\Psi \Delta\rho Z}$$

and

$$\beta = \frac{1}{Z} \left( \frac{\beta'}{\alpha'} - \Delta p_{cf} - \Delta p_\sigma \right).$$

## 6. Surface tension measurements

Surface tension measurements were performed with a Theta optical tensiometer from Ramé-Hart Instrument Co. (Netcong, NJ) using pendant and reverse pendant drop shape analysis (Fig. S5). Drops were formed using a 22 gauge stainless steel needle (Ramé-Hart) with the external phase being accommodated inside a quartz cuvette (Sigma-Aldrich). Images of drops were recorded using a CCD camera and analyzed using DROPImage Advanced software (Ramé-Hart). In pendant drop shape analysis, the drop is hanging from a downward-oriented syringe tip, while in reverse pendant drop shape analysis, the drop is lifted from an upward-pointing syringe orifice. Both methods were experimentally implemented using straight and U-shaped needles, respectively, extending vertically into the cuvette, as shown in Figs. S5a and S5b.

Drop shape analysis<sup>6</sup> relies on the Young–Laplace equation, which relates the interfacial tension to the pressure caused by the curvature of the drop

$$\Delta p = (p_{int} - p_{ext}) = \sigma \left( \frac{1}{R_1} + \frac{1}{R_2} \right)$$

where  $\Delta p$  is the difference across the interface,  $\sigma$  is the surface tension, and  $R_1$  and  $R_2$  are the principal radii of curvature (Fig. S5c). The hydrostatic equilibrium conditions require that

$$\Delta p = \Delta p_0 - \Delta\rho g z$$

where  $\Delta p_0$  is a reference pressure at  $z = 0$ ,  $\Delta\rho$  is the density difference between the internal and the external phase and  $g$  is the gravitational constant. Given that the drop is axisymmetrical, the Young–Laplace equation can be described in terms of cylindrical

coordinates  $x$  and  $z$  along with the tangent angle  $\Phi$ . Therefore, it is possible to deduct the following set of dimensionless equations

$$\frac{d\Phi}{ds} = 2 - Bo \times z - \frac{\sin \Phi}{x}$$

$$\frac{dx}{ds} = \cos \Phi$$

$$\frac{dz}{ds} = \sin \Phi$$

where  $s$  is the arc length measured from the apex, and  $Bo$  is the Bond number. The Bond number is a dimensionless quantity defined as

$$Bo = \frac{\Delta\rho g R_0^2}{\sigma}$$

where  $R_0$  is the radius at the apex. The above equations can be solved numerically for  $\sigma$  once the contour of the drop has been extracted from an image. The method uses iterative optimization to determine the parameters that best describe the extracted drop profile. A detailed account of the procedure is provided elsewhere.<sup>6</sup>

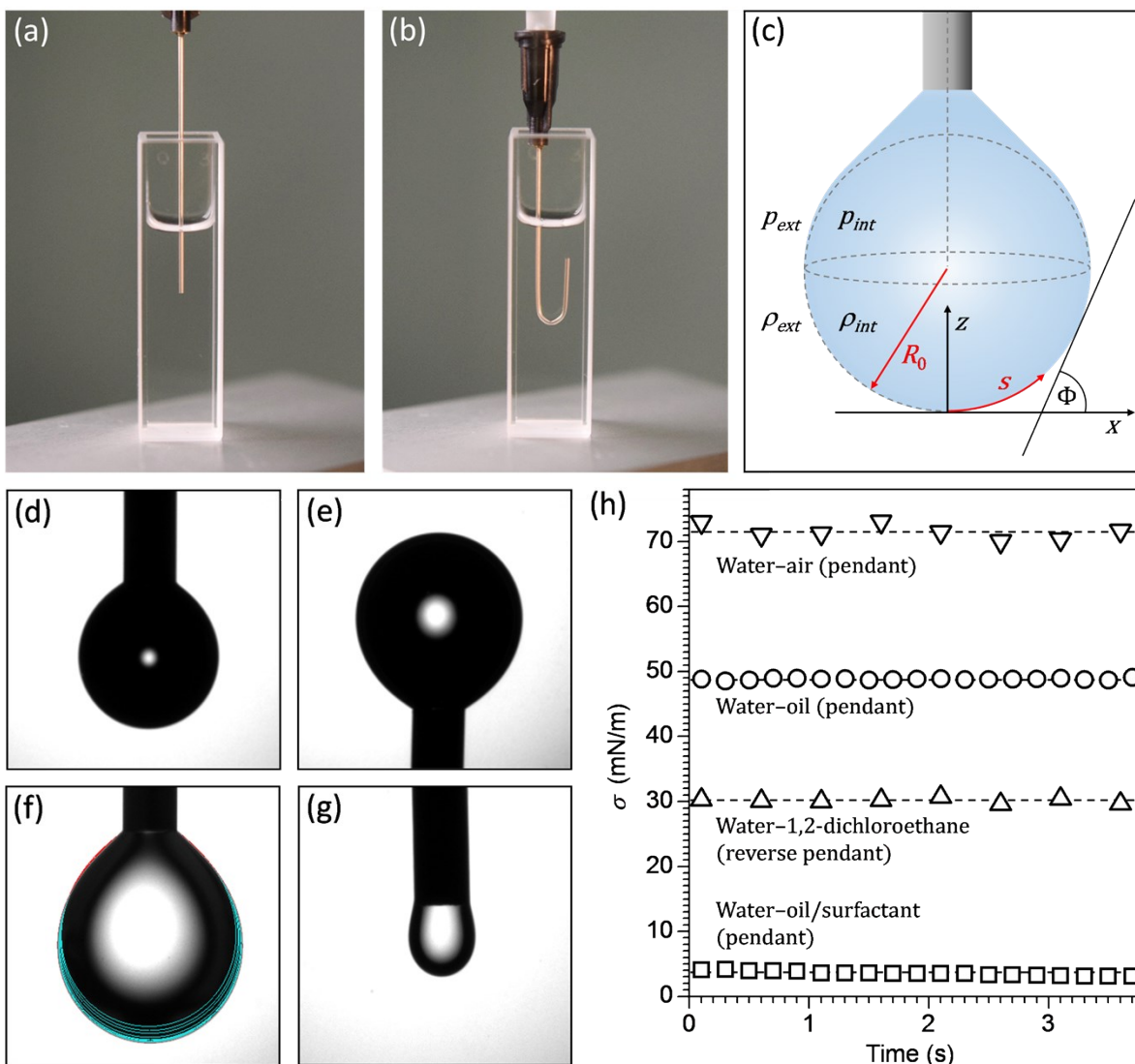


**Fig. S5** Measurement of interfacial tension using drop shape analysis. (a,b) Photographs of the syringe tips used for drop formation. The cuvette contains the external phase. (c) Schematic illustration of a pendant drop along with annotations of parameters used in the computational routine to determine interfacial tension. (d–g) Photographs of drops acquired for analysis. (d) Water in air. (e) Water in 1,2-dichloroethane. (f) Oil in water. Contour lines depict the evolution of the silhouette when the volume of the drop was expanded during the measurement (0.2 s time intervals). (g) Oil/surfactant in water. We note that drops formed with oil/surfactant detached from the needle at a significantly lower volume than drops formed with oil only (no surfactant). (h) Plot of  $\sigma$  for different interfaces obtained using the drop expansion method. Time intervals of 0.2 s were used in the drop shape analysis of water–oil and water–oil/surfactant, and 0.5 s for water–air as well as water–1,2-dichloroethane. Lines in the graph denote average values of the respective data sets. Note that drops of water in air are more sensitive to vibrations than all other systems, which can result in higher fluctuation of surface tension values.

To validate the methodology, we first performed control measurements for water–air (Fig. S5d) and water–1,2-dichloroethane interfaces (Fig. S5e) for which surface tension values are known from the literature (Table S1). Densities considered for the calculation of  $\sigma$  were 1.02237, 0.0013, and 1.2530 g/cm<sup>3</sup> for water, air and 1,2-dichloroethane, respectively. Experimental values of  $\sigma$  (Table S1) were obtained from drops for which we slightly increased the volume at the onset of the measurement. We then recorded images of the drop until equilibration of the system. Values of  $\sigma$  derived during the equilibration regime were generally the closest to the reference values. Interfacial tension for water and oil (Novec 7500 Engineered Fluid) with and without Pico-Surf 1 was also measured by analyzing drops using the expansion method (Figs. S5f and S5g). The graph in Fig. S5h shows that variation in  $\sigma$  throughout each measurement was relatively low. We typically performed 10–20 measurements per drop using time intervals of 0.5 or 0.2 s. As shown in Table S1, the presence of Pico-Surf 1 yields low values of  $\sigma$  for water–oil/surfactant interfaces.

**Table S1** Surface tension values for different interfaces determined by drop shape analysis

Interface	Method	$T$ (°C)	$\sigma$ (mN/m)	
			Measured (val. $\pm$ SD)	Best known ( val. $\pm$ SD // <sup>ref.</sup> )
Water–air	Pendant	20	72.46 $\pm$ 1.37 <sup>a</sup>	72.87 $\pm$ 0.05 // <sup>7</sup>
Water–1,2-dichloroethane <sup>b</sup>	Reverse pendant	20	30.01 $\pm$ 0.4 <sup>c</sup>	30.5 $\pm$ 0.3 // <sup>8</sup>
Water–oil	Pendant	20	48.7 $\pm$ 0.98 <sup>d</sup>	n.a.
Water–oil/surfactant	Reverse pendant	20	3.79 $\pm$ 0.61 <sup>d</sup>	3.9 $\pm$ 0.1 // <sup>9</sup>
Water–oil/surfactant	Pendant	20	3.97 $\pm$ 0.53 <sup>e</sup>	n.a.

<sup>a</sup>  $n = 40$ . <sup>b</sup> Obtained from Sigma-Aldrich. <sup>c</sup>  $n = 10$ . <sup>d</sup>  $n = 150$ . <sup>e</sup>  $n = 44$ .

## 7. References

- 1 L. Clime, D. Brassard, M. Geissler and T. Veres, *Lab Chip*, 2015, **15**, 2400–2411.

- 2 M. Geissler, K. Li, X. Zhang, L. Clime, G. P. Robideau, G. J. Bilodeau and T. Veres, *Lab Chip* 2014, **14**, 3750–3761.
- 3 L. Malic, X. Zhang, D. Brassard, L. Clime, J. Daoud, C. Luebbert, V. Barrere, A. Boutin, S. Bidawid, J. Farber, N. Corneau and T. Veres, *Lab Chip*, 2015, **15**, 3994–4007.
- 4 L. Malic, J. Daoud, M. Geissler, A. Boutin, L. Lukic, M. Janta, A. Elmanzalawy and T. Veres, *Analyst*, 2019, **144**, 6541–6553.
- 5 J.-F. Gravel, M. Geissler, S. Chapdelaine, K. Boissinot, B. Voisin, I. Charlebois, H.-P. Poirier-Richard, A. Grégoire, M. Boissinot, M. G. Bergeron, T. Veres and D. Boudreau, *Microfluid. Nanofluid.* 2014, **16**, 1075–1087.
- 6 J. D. Berry, M. J. Neeson, R. R. Dagastine, D. Y. C. Chan, R. F. Tabor, *J. Colloid Interface Sci.*, 2015, **454**, 226–237.
- 7 N. R. Pallas and Y. Harrison, *Colloids Surf.* 1990, **43**, 169–194.
- 8 E. Smirnov, P. Peljo, M. D. Scanlon, F. Gumy and H. H. Girault, *Nanoscale*, 2016, **8**, 7723–7737.
- 9 F. Schuler, F. Schwemmer, M. Trotter, S. Wadle, R. Zengerle, F. von Stetten and N. Paust, *Lab Chip*, 2015, **15**, 2759–2766.